Intruding gravity currents and their recirculation in a rotating frame: Numerical results

Achim Wirth, Maria Eletta Negretti

Intruding gravity currents and their recirculation in a rotating frame: numerical results

Achim Wirth, Maria Eletta Negretti

Univ. Grenoble Alpes, CNRS, Grenoble INP, LEGI, 38000 Grenoble, France

Abstract

Using a set of direct numerical simulations (DNS) we investigate the circulation of a buoyancy driven experiment in a circular rotating tank. The initial density structure is a two-layer stable-stratification. The water is densified at 32 points at the upslope side of a circular incline and flows downward as a gravity current before it intrudes to the interior along the interface between the two layers. The water above recirculates to the densification points.

When the buoyancy production is lower than the maximal Ekman transport, the gravity current proceeds in the laminar Ekman layer. In the opposite case, the water cascades down the incline in a no-stationary dynamics, turbulent transport becomes important and the boundary layer is thickened. The thermal wind relation applied to the tangential velocity averaged-along-the-slope predicts the density structure averaged-along-the-slope in the domain.

When the densified water arrives at the interface it flows along the slope in the cyclonic direction, in a geostrophically adjusted deep boundary current. The distance of the boundary current from the slope is given by inertial overshoot of the Ekman current due to the self advection by the inertia. When this distance is small the boundary current is close to the slope and subject to boundary friction. In the opposite case the boundary current evolves detached from the boundary. The intrusion along the interface, in the (negative) radial direction, is slow, as the intruding distance is proportional to the square-root of time.

Email address: achim.wirth@legi.cnrs.fr (Achim Wirth)

The recirculation in the upper layer is close to a geostrophic equilibrium. Its quasi-geostrophic evolution is due to the compression of the water column, caused by the gravity and intruding currents, below. This leads to a large-scale anti-cyclonic circulation in the upper layer. When the associated geostrophic surface pressure gradient exceeds the pressured gradient due to the dense water on the slope, the Ekman transport is upslope.

A special emphasis is put on the interactions of the three phases of the circulation: gravity-current, intrusion and recirculation. The circulation and the mixing of density and momentum in the gravity current determine the water-mass properties in the deep boundary current. Both determine the recirculation. The recirculation leads to an increasing anti-cyclonic circulation above the gravity current which, through the corresponding surface pressure gradient, reduces and finally blocs the downslope movement in the Ekman layer.

Keywords: rotating gravity current, slope current, intrusion, recirculation

1. Introduction

Density differences in fluids created through differential heating by the sun, or other heat sources, are, combined with the gravitational acceleration, the major source of motion in environmental fluids. The lighter fluid is accelerated upward and heavier fluid downward. The vertical acceleration and buoyancy transport leads to horizontal pressure gradients and horizontal motion. When the vertically moving fluid encounters a solid boundary a gravity current is created. Here, we discuss only descending, dense, gravity currents. The physics of rising, buoyant, gravity currents is identical, when density differences are small (when the Boussinesq approximation applies). The gravity current moves along the boundary until its downward motion is halted by the bottom or by a fluid of higher density and its motion is redirected to horizontal. The circulation is influenced by turbulence, which mixes density and momentum, bottom friction, the rotation of the Earth and many other processes ([1], [2], [3], [4], [5], [6]).

The difference between atmospheric and oceanic gravity currents is that the

former evolve mostly on time scales shorter than a day, while the descend of the latter is slower, takes several days and the rotation of the Earth plays a governing role.

Oceanic gravity currents have been extensively studied in the past. These studies were mostly concerned with the downward motion and its arrest at the ocean floor. Most oceanic gravity currents are, however halted in their downward propagation by a denser water mass and do not reach the ocean floor. Observed examples are the outflows at Gibraltar [7], Bab-el-Mandeb [8], the strait of Hormus [9], into the Baltic Sea [10], or the overflows at the Denmark Strait [11] and in the Faroe Bank Channel [12], as well as the gravity currents in the Gulf of Lions [13]. Laboratory experiments on rotating gravity currents have been performed by [2], [14], [15], [16], [17] and many others. Numerical simulations of idealised and observed gravity currents are numerous, see i.e. [18], [19], [20], [21] and references therein. The laboratory experiments and the numerical simulations mentioned, do not consider the intrusion of rotating gravity currents, while the observed gravity currents mentioned above are all intruding at one point, stop their downward motion along the slope.

In the present work we are concerned with a gravity current, its intrusion when the downslope propagation is arrested by a layer of dense water and the recirculation in the water above, as well as the interaction of these three phases. To this end we have envisioned a physical model which is realised on the Coriolis platform at LEGI, Grenoble, France and use a mathematical model thereof, the hydrostatic equations of geophysical fluid dynamics, which are integrated numerically using the CROCO ocean code. The aim is to set up a hierarchy of experimental, mathematical and numerical models, to further our understanding of the average circulation of oceanic gravity currents that flow downslope into a stratified environment, intrude into the interior and lead to a recirculation of the superposing water-masses. The emphasis in the present work is on the large scale circulation leaving the dynamics of the turbulent fluctuations for future publications. Such separation between an averaged circulation and fluctuations in a non statistically-stationary dynamics is made possible by the

circular symmetry of the experiment, which allows for averaging along the angle ϕ (see Fig. 1).

Note that the present configuration is substantially different from a lock release gravity current in a rotating frame on a flat ground (see i.e. [26] [27]) we densify the water continuously, with no initial shock or loss of balance (neither hydrostatic nor geostrophic). In our experiment balance is mainly broken by small scale friction processes. The radius at which the injection sites are placed is large and plays a subdominant role. Indeed the geometry is chosen so that the process approaches an infinitely long gravity current, dominated by hydrostatic and geostrophic balance.

The results from the laboratory experiment will be presented elsewhere [22]. The goal of the numerical simulations is to perform controlled experiments that help to understand the more involved, less controlled and only partially observed phenomena in the laboratory experiments, rather than creating a numerical twin. The here discussed numerical simulations are therefore a component of the hierarchy of models discussed above, connecting in a systematic way analytic solutions to eddying simulations, to laboratory experiments and environmental observations.

2. Experiment and qualitative description

A top and a side view of the experiment is presented in figures 1 and 2, respectively. The tank performs a uniform rotation with the Coriolis frequency $f = 2\Omega = 4\pi/T$, where T is the period of rotation. Initially there are two water masses. The upper of density ρ_1 and layer thickness of h_1 superposes a denser bottom-layer of density ρ_2 and thickness h_2 (see table 1 for values). At 32 "source points" (marked by black dots in the figs. 1 and 2), equidistantly distributed at a distance of 6.25 m from the centre, the water is accelerated along the inclined plane of slope $\alpha = 0.1$ at an angle of $\varsigma = -45^o$ with respect to the down slope direction. The acceleration force is constant in time and equal in all experiments expX2, it is tenfold smaller in exp01 and a hundred-fold smaller in

exp000. The oblique acceleration rather than a downslope acceleration is used to speed-up geostrophic adjustment of the resulting rotating gravity current. The volume of the pushed water is M_S. The density of the source water is given, as usually done in oceanography, by its dimensionless sigma-value $\sigma_S = \rho_S - 1000$, where ρ_S is measured in kg m^{-3}). It is increased by $\Delta\rho_S = 10$ kg m^{-3}, that is $\Delta S = 10$ at the "source points" leading to an overall buoyancy production rate:

$$B_S = M_S g(\rho_S - \rho_1)/\rho_S, \tag{1}$$

where g is gravity. The total sigma value of a water mass, that has a certain concentration of source water and water form layer 1 and 2, is: $\sigma = \sigma_S + \sigma_2$, note that $\sigma_1 = 0$. The density (in kg m^{-3}) is therefore $\rho = 1000 + \sigma_S + \sigma_2$.

Please note that for numerical reasons (see section 4) no water is added during the experiments, the total volume stays constant throughout the experiments. This differs from the laboratory experiments presented in [22], where dense water is injected. The circulation is governed by the large scale mass fluxes, through convergence and divergence and is therefore different between the numerical results presented here and the laboratory experiments presented in [22]. More precisely, the dynamics above the gravity current is governed by the recirculation of the water masses, in both the laboratory experiment and the numerical experiment. The recirculation is different in the laboratory experiment due to the injection of water. Smaller scale processes are relatively more independent of the large-scale balances and the corresponding numerical results will be compared to the laboratory experiments elsewhere.

The source water flows as a gravity current towards the centre along the topography and is further deviated to the right by the Coriolis force leading to a cyclonic circulation. When it encounters the bottom layer, the downslope motion stops and the source water intrudes along the interface and forms a boundary current proceeding cyclonically along the slope. Instabilities of this intruding boundary current might lead to intermittent intrusions of source water towards the centre of the domain. When the source water proceeds towards the centre as it travels downslope and intrudes, it compresses the water col-

umn above, leading to an outward flow, towards the source points, in the upper layer, called recirculation (see figure 2). This recirculating flow is deviated by the Coriolis force to the right leading to an anti-cyclonic circulation. The circulation is therefore separated in three phases operating in different areas: the gravity current on the slope, the intrusion at the interface and the recirculation above the gravity current and the intrusion. Making this qualitative description quantitative is hampered by the presence of turbulent fluxes of mass and momentum that cannot be related to the average quantities in a straight forward way, a problematic which is referred to as the closure problem.

Due to the periodicity of the experiment along concentric circles, with 32 repetitions, averages can be taken along the angle ϕ, the almost homogeneous direction in the experiment. This allows to distinguish between a spatial average along ϕ called "circulation", which is a function of the radius r, the vertical coordinate z and time t. The deviations from this average are called "fluctuations". The origin of fluctuations can be either due to the discreteness of the point sources or appear spontaneously, or is a combination of both. It is seen in the laminar and turbulent experiments that with the downslope distance from the source sites, the gravity current evolves towards (statistical) homogeneity in the ϕ-direction, "forgets" about the periodicity and details of the source. Determining the evolution of the circulation is the purpose of this communication. The dynamics does not reach a statistically-stationary state as, both, the circulation and the moments of fluctuating quantities averaged along ϕ are evolving in time

For numerical reasons, we do not analyse the current around the 32 sites where dense water is generated as, the mode of generation mimics the source of the laboratory experiment as closely as possible but is not identical and, furthermore, has no correspondence in oceanic context. In the environment the densification of air and water happens over large areas, orders of magnitude larger than the area of the gravity current, which is a small-scale phenomena in the global ocean circulation. In laboratory and numerical experiments, dedicated to the dynamics of gravity currents, we do not have the space available

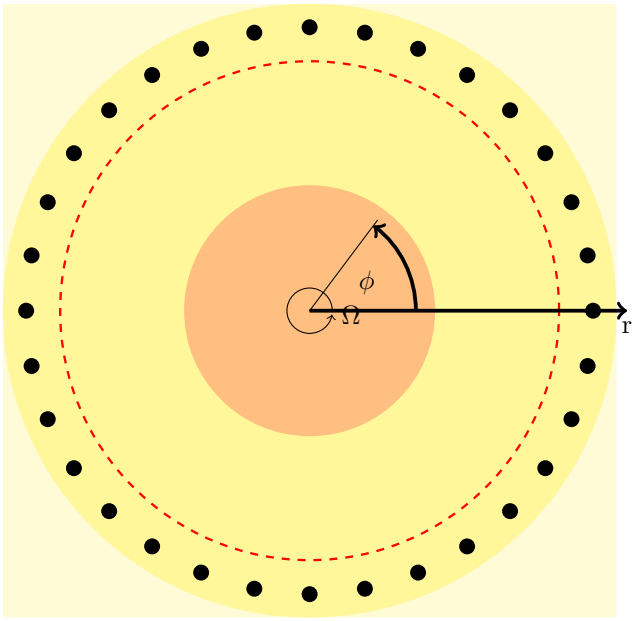

Figure 1: Birds eye perspective of the experiment. The square (side length of 13.5 m) represents the domain, the inner orange circle (radius $r = 2.75$ m) is $h_{max} = 0.51$ m deep, the light yellow corners are $h_{min} = 0.11$ m deep and the dark yellow ring represents the constant slope ($\tan\alpha = 0.1$) area. The 32 black dots ($r = 6.25$ m) are the sites at which the fluids density is increased and accelerated downward. The circulation is analysed within the red dashed circle ($r = 5.5$ m).

.

to closely mimic the densification. We therefore focus on the common features of gravity currents, the downslope motion and the intrusion and restrict our analysis to a region within a radius of 5.5 m.

3. Theory

We use a polar coordinate system where all variables depend on the radius, angle, height and time, respectively (r, ϕ, z, t). The unit vector in the local radial direction is $\hat{r}$ and $\hat{\phi}$ is the unit vector in the locally tangential direction to the platform centre. The velocity components in the polar coordinates are denoted by $u_r, u_{\hat{\phi}}, w$.

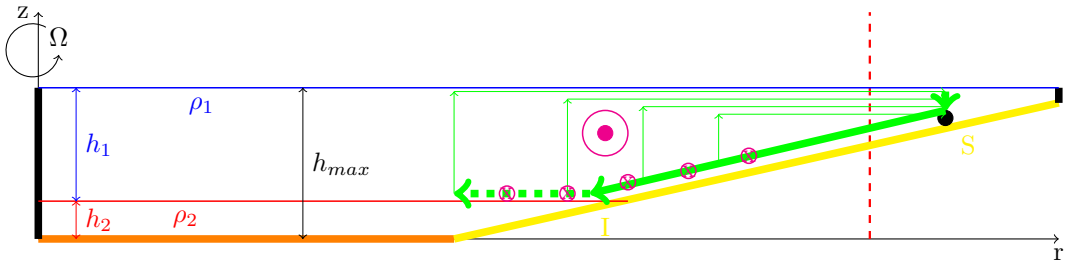

Figure 2: Sketch representing the circulation in the experiment in a $(r-z)$ plane of the domain, where all variables are averaged along the angle ϕ, that is along concentric circles. Blue line is the free surface, red line the interface at the beginning of the experiment, separating fluids of density ρ_1 and ρ_2. See section 1 for more details. The green arrows show the large scale circulation in the $(r-z)$ plane $(\langle u_r \rangle_\phi, \langle w \rangle_\phi)$. Magenta symbols give the circulation in the ϕ direction $(\langle u_{\hat{\phi}} \rangle_\phi)$. The water is densified to ρ_s and accelerated at the source point S, from which it flows down and follows the slope in a cyclonic direction, entraining surrounding water of density ρ_1 (this phase, given by the thick-full green line, is called the gravity current). When the water is at the intruding point I it has a density $\rho_1 < \tilde{\rho}_s < \rho_2$. The water intrudes (dashed green line) while the Coriolis force accelerates it in the tangential direction and the water proceeds cyclonically close to the slope (this phase, given by the thick-dashed green line, is called the intrusion). Above the gravity current and the intrusion the water moves outward and turns anti-cyclonically (this phase, given by the thin green lines, is called the recirculation). See section 6 for more details. The circulation is analysed left of the red dashed line, away from the source point S.

The almost homogeneity of the experiment along the angle ϕ allows to separate the dynamics in a circulation and fluctuations. To this end we denote the averages over a circle of a given radius, of any variable a by $A(z,r,t) = \langle a(z,r,\phi,t)\rangle_\phi$. This averaging allows to obtain the circulation $A(z,r,t)$ in the experiment. The fluctuations are then $a'(z,r,\phi,t) = a(z,r,\phi,t) - A(z,r,t)$, of which we analyse the moments, by again averaging along the angle ϕ. Notice, that the circulation and the statistics of the fluctuations, moments of fluctuating quantities, evolve in time. The dynamics does not reach a statistically stationary state, but the homogeneity along ϕ allows for averaging over turbulent fluctuations and obtaining an averaged circulation and average turbulent fluxes.

As described above, we can distinguish three phases in the circulation: gravity current, intrusion and recirculation. The theory necessary to describe each of the phases will be discussed in the following subsections.

3.1. Gravity current

On its downslope propagation the gravity current continuously adjusts to the rotating frame, passes from a non-rotating downslope gravity current to a cross-slope rotating gravity current in geostropic equilibrium (see [14], [3], [6]). When a laminar gravity current of density ρ_s is flowing through an inert ocean of density ρ_1 its circulation approaches geostropic equilibrium, in which the cross-slope velocity $u_{\hat{\phi}}$ is obtained by a balance between the downslope acceleration, which is given by the product of the topographic slope α and the reduced gravity $b_S = g(\rho_s - \rho_1)/\rho_s = 9.71 \cdot 10^{-2}\text{m s}^{-2}$, and the inverse of the Coriolis acceleration. This balance allows to define a geostrophic velocity associated to the slope and the density difference:

$$u^g = u_{\hat{\phi}} \quad = \quad \frac{\alpha b_S}{f_0} = 9.25 \cdot 10^{-2}\text{ms}^{-1}, \tag{2}$$

where the numerical value corresponds to the reference experiment exp02. In our experiments the water above the gravity current is in motion and the density varies smoothly. For such case the geostrophic equilibrium generalises to the

thermal-wind relation:

$$\partial_z u^g_{\hat{\phi}} = -\frac{g\partial_r \rho}{f\rho} \quad (3)$$

$$\partial_z u^g_r = \frac{g\partial_{\hat{\phi}} \rho}{f\rho}. \quad (4)$$

The thermal wind relation is used in section 6.1 to show that the tangential component of the circulation is always close to geostrophic equilibrium even within the gravity current. When the thermal wind-relation applies to the circulation, it has no radial or downslope velocity $\langle u^g_r \rangle_\phi = 0$. This follows from Eq. (4) as the average along ϕ of the r.h.s. vanishes and $\langle u^g_r \rangle_\phi = 0$ at the centre, by definition. It follows that for a downslope propagation of dense water we need and/or: fluctuations, friction, non-linearity, time dependence.

Due to bottom friction, an Ekman layer appears at the bottom of the gravity current in which dense water is transported downward. The structure of the gravity current is composed of a thick vein superposing a thin frictional Ekman layer, as shown in [14], [3], [6]. In the Ekman layer the cross-slope velocity is reduced by friction, the Coriolis force no longer balances the downslope acceleration and the dense water descends. When the velocity above the gravity current vanishes, the downslope transport is proportional to the shear-force at the slope. The (thick) part of the gravity current not directly subject to frictional forces is called the vein, it is influenced by the Ekman layer dynamics from below through Ekman pumping ([3], [6]).

Derived parameters for a constant viscosity law are: the thickness of the Ekman layer δ_{Ek}, the shear vector τ, the downslope Ekman transport T_{Ek}, the total downslope Ekman transport M_{Ek} in the experiment, and the total downslope buoyancy transport B_{Ek}:

$$\delta_{\mathrm{Ek}} = \sqrt{\frac{2\nu}{f_0}} = 4.37 \cdot 10^{-3}\mathrm{m} \quad (5)$$

$$\tau = (\tau_r, \tau_{\hat{\phi}}) = \nu \frac{u^g}{\delta_{\mathrm{Ek}}}(-1,1) = \sqrt{\frac{\nu}{2f}} \alpha b_S (-1,1) \quad (6)$$

$$T_{\mathrm{Ek}} = \frac{\tau_r}{f} = -\frac{\delta_{\mathrm{Ek}}}{2} u^g = -\alpha b_S \sqrt{\frac{\nu}{2f^3}} \quad (7)$$

$$M_{\mathrm{Ek}} = LT_{\mathrm{Ek}} = 2\pi r\alpha b_S\sqrt{\frac{\nu}{2f^3}} \approx 6.35\cdot 10^{-3}\mathrm{m}^3\mathrm{s}^{-1}, \quad (8)$$

$$B_{\mathrm{Ek}} = \sigma_S M_{\mathrm{Ek}} \approx 6.35\cdot 10^{-2}\mathrm{kgs}^{-1}, \quad (9)$$

where numerical values refer to the reference exp02 (for which $f = f_0$, see tabs. 1 and 2). The values of M_{Ek} and B_{Ek} give the maximal amount of volume and kg of salt that can be transported downslope by the Ekman layer. The value for the maximal buoyancy transport, does not take into account the mixing and diffusion at the source and on the way down the incline. The Ekman layer is subject to diffusion so its downslope buoyancy anomaly reduces over a characteristic length scale:

$$l_{Ek} = u^g\frac{\delta_{Ek}^2}{\kappa} = \frac{2\nu\alpha b_S}{f^2\kappa} \approx 1.4\mathrm{m}. \quad (10)$$

The determining parameter is the flux Ekman number $D_{Ek} = B_{\mathrm{Ek}}/B_S$ comparing the buoyancy the Ekman dynamics can transport downward, to the source buoyancy anomaly B_S (see eq. (1). When the source rate exceeds the value ($D_{Ek} < 1$), buoyancy accumulates and the thickness of the vein increases.

When the vein becomes unstable, other, time-and-space dependent, processes can lead to a downward buoyancy-transport. In this case the transport happens at a thick boundary layer, it is turbulent and it cascades down the incline. The thickening of an accelerating boundary layer in a rotating frame was analytically shown by [23] for an idealised case. For a discussion of cascading in the ocean from observations and its representation in realistic numerical simulations, I refer to [24] for the Arctic and to [25] for the Mediterranean. Both works emphasise the importance of the the topographic structure on the cascading, a subject that is not considered here.

3.2. Intruding current

Due to the periodicity in the ϕ direction there is no average pressure gradient in this direction and therefore also no geostrophic radial circulation, $\langle u_r^g\rangle_\phi = 0$. Non-linearity or friction can relax the geostrophic constraint and allow for a circulation in the radial direction. Non-linearity allows for an inertial overshoot,

while friction leads to a radial circulation on the slope in Ekman layers and between water masses of different densities in interfacial Ekman layers.

When the gravity current water arrives at the interface it has a density anomaly $b_{\rm in}$. If the downward transport, given by Eq. (7), is done by the Ekman layer the corresponding downslope velocity in the negative r-direction is $u^{b_{\rm in}}/2$. If the current performs an inertial overshoot it penetrates a maximal distance

$$l_{\rm iner} = \frac{u^{b_{\rm in}}}{2f} = \frac{\alpha b_{\rm in}}{2f^2} \tag{11}$$

into the interior while turning anti-cyclonically.

The numerical integrations, discussed below, show that dense water follows the slope, it resembles a deep boundary current that grows in breadth and thickness due to a constant supply of dense water by the gravity current. The thermal wind relation of Eq. (3) relates slope of the pycnocline in the radial direction to the velocity of the deep boundary current and therefore to $b_{\rm in}$. When the deep boundary current grows in breadth, extending away from the boundary, it also has to increase its vertical extension. A constant influx of dense water then leads to an intrusion where the square of the intruding distance is proportional to time: $\tilde{x}_{\rm in}^2 = \gamma t$, where γ is a constant. Note, that a proportionality of the intrusion to the square-root of time does not mean that the intrusion is done by diffusive processes. It occurs when the cross-section of the deep-current preserves its shape while being supplied by a constant influx of dense water.

3.3. Recirculation

In the upper layer, which is not directly subject to strong frictional forces, the dynamics can be described by the conservation of potential vorticity q:

$$\frac{d}{dt}q = (\partial_t + u_r\partial_r + u_{\hat{\phi}}\partial_{\hat{\phi}})\left[\frac{\zeta + f}{h}\right] = 0, \tag{12}$$

$$\zeta = \frac{u_{\hat{\phi}}}{r} + \partial_r u_{\hat{\phi}} - \partial_{\hat{\phi}} u_r, \tag{13}$$

where ζ is the vorticity. When we consider the potential vorticity of the circulation by averaging along ϕ ($\langle\rangle_\phi$) the advection of potential vorticity along

ϕ disappears. Note that it is in the ϕ direction that we have the strongest large scale advection. When we further neglect the radial advection (an approximation which will be justified by the data analysis in subsection 6.3) Eq. (12) simplifies to a balance between the local change of vorticity and the local vortex stretching:

$$\partial_t \langle \zeta \rangle_\phi = \langle \frac{\zeta + f}{h} \partial_t h \rangle_\phi \tag{14}$$

We further average the dynamics in a surface layer down to a depth $h_0 = 0.1$ m, by using the average $\langle \zeta \rangle_{h_0}$ and obtain a relation between the change of vorticity and the vertical velocity $w(-h_0)$ (vortex stretching):

$$\langle \partial_t \zeta \rangle_{\phi,h_0}(r,t) \approx \frac{\langle \zeta \rangle_{\phi,h_0} + f}{h_0} \langle -w(-h_0) \rangle_\phi \tag{15}$$

where we used $w(-h_0) = -\partial_t h|_{-h_0}$, which measures the (negative) vortex stretching of the above water column. The recirculation dynamics is forced by vortex stretching represented by the vertical velocity, which is measured in the experiments.

When horizontal advection of potential vorticity is neglected we obtain integrating Eq. (15) in time and using Eq. (13):

$$\frac{\langle u_{\hat{\phi}} \rangle_{\phi,h_0}(r,t)}{r} + \partial_r \langle u_{\hat{\phi}} \rangle_{\phi,h_0}(r,t) = \frac{f \Delta h(r,t)}{h_0} \tag{16}$$

$$\text{with :} \qquad \Delta h(r,t) = \int_0^t \langle w(-h_0) \rangle_{\phi,h_0} dt'. \tag{17}$$

This shows that in the recirculation area a clockwise circulation grows constantly in time, when turbulent fluxes are neglected. The Ekman transport becomes upslope at a time t_{up}, when $u_{\hat{\phi}}(t) < -u^g$, that is, when the geostrophic surface pressure gradient, pushing the water upslope, exceeds the downslope gravitational-acceleration of the gravity current water.

3.4. Turbulent parameters

Non dimensional geometric parameters are the slope α and the stretching parameter $\Gamma = \alpha l/d$, where l is length of the slope and d the average depth. The Prandtl number compares viscosity to diffusivity $Pr = \nu/\kappa = 20/3$.

The turbulent regimes are usually characterised by the Reynolds number Re, the Richardson number Ri, the Froude number Fr and the Rayleigh number Ra. If we base these numbers on the Ekman-layer thickness δ_{Ek} they are related:

$$Re = \frac{u^g \delta_{\mathrm{Ek}}}{\nu} = \frac{\sqrt{2} b_S}{\sqrt{f^3 \nu}} \approx 416 \tag{18}$$

$$Ri = \frac{\delta b_S}{(u^g)^2} = \frac{\sqrt{2\nu f^3}}{\alpha b_S} = \frac{2}{\alpha Re} = Fr^{-2} \approx 4.82 \cdot 10^{-4} \tag{19}$$

$$Ra = \frac{b_S \delta_{\mathrm{Ek}}^3}{\nu\kappa} = 2RePr \approx 5545, \tag{20}$$

where numerical numbers correspond to the reference experiment exp02. Note, that with increasing Coriolis parameter, both, the geostrophic velocity and the Ekman-layer thickness decrease and so does the Reynolds number based on Ekman dynamics. The Ekman number Ek is the square of the thickness of the Ekman layer divided by the square of the thickness of the gravity current.

4. Direct Numerical Simulations (DNS)

The model used is the hydrostatic version of CROCO (https://www.croco-ocean.org) which solves the free surface, primitive equations. Its dynamical kernel is described in [28]. The simulations of the domain are performed at a horizontal resolution of $(13.5 \text{ m } /1024)^2$ and there are 64 σ-levels in the vertical (finest resolution of the first level varies from 1 mm at the upper part of the incline to 5 mm at the deepest part of the domain). The boundary condition at the bottom is no-slip. The time-step is $\Delta t = 3 \cdot 10^{-3}$ s.

Since we found that increasing the volume by injecting fluid as it is done in the experiments on the Coriolis Platform leads to a numerical instability at the free surface (except for very weak injection rates). Therefore we choose to accelerate the water above the source points, 32 grid points at $r = 6.25$ m in the lower 2.5 cm, at an angle of -45° to the radial direction. The acceleration force is constant in time and equal in the experiments expX2 (X=0,1,2,3,4). The total accelerated water-mass is increased by a density of 10kg m^{-3}. The resulting buoyancy flux is given below, for each experiment. No water is injected and

the total volume stays constant throughout the experiments. The acceleration and densification procedure can not be easily implemented in the laboratory experiment and the laboratory experiment and the numerical experiment differ in this aspect. We emphasise, that such kind of forcing can be implemented, at high financial costs, in a laboratory experiment by putting pumps and adding salt at the source points. By changing the injection mode in the numerical experiments with a low injection rate no dependence of averaged quantities on the injection mode was observed further downstream of the injection points

The advection scheme are 5th order in space for tracers and momentum in the horizontal and vertical direction. We performed direct numerical simulations (DNS) using the molecular values of water for the viscosity $\nu = 1. \cdot 10^{-6}\mathrm{m}^2\mathrm{s}^{-1}$ and the thermal diffusivity $\kappa = 1.5 \cdot 10^{-7}\mathrm{m}^2\mathrm{s}^{-1}$. We are aware that the numerical diffusion may exceed the explicit values, but as the implementation of the equations in the CROCO code is consistent, the solutions will converge as the resolution in space and time is refined.

5. Experiments performed

We performed seven experiments all extending over a time interval of at least $t = 3000$ s. The physical parameters of the reference experiment exp02 are given in table 1. The parameters varied between experiments are the source rate and the rotation rate. For experiments exp00 and exp01 we reduced the source rate by a factor of 100 and 10, respectively. The low source rates lead to an almost linear evolution of the dynamics. The other experiments all have a high source rate, but different rotation periods of $T = 30$ (exp32), 60 (exp12), 120 (exp02) and 240 (exp42). Experiment (exp22) has no rotation, that is $T = \infty$. The early evolution of the density structure in the first grid point above topography is given in Fig. 3 for the low and the very high rotation cases. In the centre of the domain the water mass of density ρ_2 is seen in all experiments and at all times. In the low rotation rate experiment the oblique injection is seen at the source and the dense water moves down in the Ekman layer at all times during

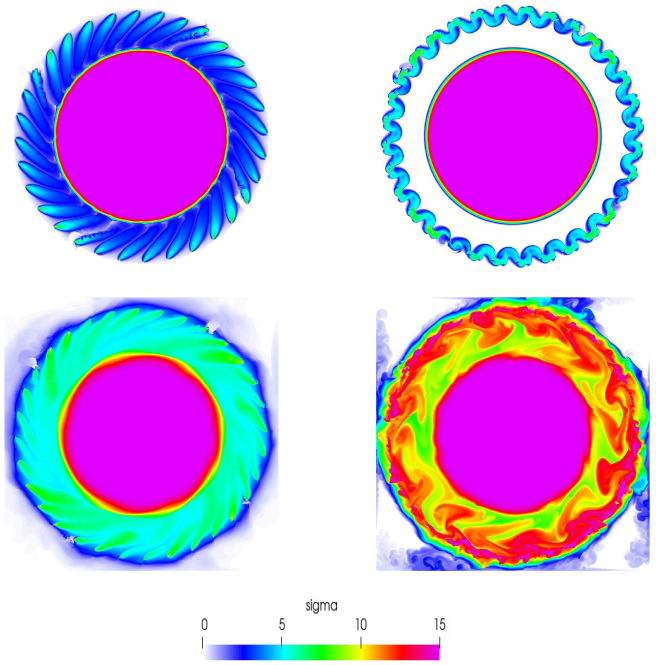

Figure 3: Fig. shows the density (sigma value) in the first grid point above topography at $t = 120$ s (upper) and $t = 3000$ s (lower), for the low rotation experiment (exp42, left) and the very high rotation experiment (exp32, right). The Ekman layer stays laminar in the low rotation experiment but becomes turbulent in the very high rotation case.

the experiment. In the highest rotation case the Coriolis force deviates the flow to the right and the dense water turns upslope before moving principally along the slope due to geostrophic adjustment. At later times the dynamics is turbulent down to the the lower boundary.

325 The parameters varied as well as the geostrophic velocity and the Ekman layer thickness, using formulas from section 3 are given in table 2.

6. Results

We distinguish four different areas of the dynamics in our experiment. One is the source region around the injection points. The mode of source implemented

ν	κ	$r_{\max}$	$r_{\min}$	r_S	$h_{\max}$	$h_{\min}$
10^{-6} m^2 s^{-1}	$1.5 \cdot 10^{-7}$ m^2 s^{-1}	6.75 m	2.75 m	6.25 m	0.51 m	0.11 m
h_1	h_2	ρ_1	ρ_2	α	f_0	b_S
.35 m	.16 m	1000 kg m^{-3}	1015 kg m^{-3}	0.1	$\frac{4\pi}{120s} \approx 0.105s^{-1}$	10^{-1} m s^{-2}

Table 1: Experimental parameters common to all experiments performed.

Exp.	comment	rotation f/f_0	u_g / 10^{-2} m s^{-1}	δ_{Ek} / 10^{-3} m	B_S / 10^{-3} kg s^{-1}
exp00	very low source	1	9.25	4.37	$1.65 \cdot 10^{-2}$
exp01	low source	1	9.25	4.37	$2.07 \cdot 10^{-1}$
exp02	reference	1	9.25	4.37	6.40
exp12	high rotation	2	4.63	3.09	4.46
exp22	no rotation	0	na	na	12.0
exp32	very high rotation	4	2.31	2.18	5.52
exp42	low rotation	1/2	18.5	6.18	9.35

Table 2: Parameters changed between the 7 experiments: the rotation rate, the corresponding geostrophic velocity and the Ekman layer thickness are calculated based on imposed parameters. The buoyancy transport B_0 at $r = 5.5$ m and $t =$3000 s, is an observed quantity varying in time, not known prior to the experiment.

in the numerical model is close to the injection in the laboratory experiment performed on the Coriolis platform, which differs from the source of gravity currents in the natural environment (see section 2). The strongly turbulent dynamics in this area consisting of mostly cyclonic eddies, depends on the details of the source, lacks generality and will not be discussed here. We will consider the downslope movement of the dense water in a gravity current on the slope at a distance from the source sites, when the dynamics has "forgotten" about the details of the densification process. This area starts about half a meter downslope from the sources and extents down to the interface at which the dense water intrudes to the interior along the interface. The downslope and intruding current pushes away the surrounding water that recirculates to the source region above the gravity current, as shown in Fig. 2.

The three phases considered: gravity current, intrusion and recirculation, take place in distinct areas of the experiment. The circulation in each of the phases is analysed in the following subsections, using data from the numerical experiments.

6.1. Gravity current

The density in the lowest level above the bottom is given in Fig. 3 for the low (exp42) and the very high rotation (exp32) cases. While in the low rotation case the laminar Ekman dynamics prevails during the experiment, the bottom boundary layer becomes turbulent in the very high rotation case. In Fig. 4, right column, the total radial buoyancy transport $T_s(z) = \langle u_r \sigma_S \rangle_\phi$ is plotted for three values of the radius over the slope at $t = 3000$ s, as a function of the vertical direction z, for three different experiments. For the low rotation, the downward transport is performed by the thin Ekman layer as seen in exp02 and exp42 (upper- and middle-right panel of Fig. 4) (called Ekman case in the sequel). The downward and inward transport depends on the shear force exerted by the bottom boundary es described in section 3. Just above the gravity current there is a counter flow and the detrained salty water flows upward and outward, leading to an upward and outward transport of dense water (see Fig. 4). The

upslope transport also shows that the gravity current is detraining, which leads to a decrease of the downslope buoyancy transport with the downslope direction, which can be seen in the same figure looking at profiles for different values of the radius r. The total buoyancy transport can be separated into a part due to the circulation $T_s^c(z) = \langle u_r \rangle_\phi \langle \sigma_S \rangle_\phi$ and a fluctuating part $T_s^f(z) = T_s(z) - T_s^c(z)$. For the Ekman dynamics the fluctuating part is negligible which shows that the dynamics is close to laminar (Fig. 4) and that the homogeneity due to the 32 source points decreases in the downslope direction and has almost disappeared 1 m downslope of the source sites.

Using the thermal wind relation (eq. 3) the density structure averaged along the angle ϕ can be obtained from the tangential velocity averaged along the angle ϕ, as can be seen in the middle column of Fig. 4. Note that the thermal wind relation does not apply to non-averaged quantities due to the presence of inertia-gravity waves.

In the very high rotation case (exp32) the anti-cyclonic circulation in the recirculation area becomes so strong, that also near the bottom the circulation is anti-cyclonic and therefore the Ekman transport is upslope. This can be seen in the lower-right panel of Fig. 4 and in Fig.6, where at the upslope location ($r = 5.53$m) the tangential velocity $u_{\hat{\phi}}$ averaged along the angle ϕ is always negative which leads to an upslope Ekman-transport. In terms of the thermal wind relation this means that the horizontal density variations in the fluid are not strong enough to counter-balance the geostrophic pressure gradient at the surface. When the volume of the water densified at the source per time exceeds the downward Ekman transport the dense water accumulates for some time at the upper part of the incline, until it proceeds downward above the Ekman layer, as can be seen for exp32 in Fig. 4. No laminar solution is available and the fluctuating buoyancy transport is performed in a thick turbulent boundary layer. This behaviour will be called "cascade dynamics" in the sequel. In the same figure we also see that the turbulent transport is always down slope. The cascade dynamics has a turbulent transport, which is strongly increased. The downward transport is very intermittent in time and consists of avalanches or

bursts (not shown). Note that also in the cascading dynamics the circulation part of the downslope transport is confined to the bottom Ekman layer, this can be seen by looking at the difference of the full line and the dashed line in the lower-right panel of Fig. 4.

6.2. Intruding current

For the lowest rotation case the density anomaly of the source water $\langle \sigma_S \rangle_\phi$ as well as the isolines of $\langle u_{\hat{\phi}} \rangle_\phi$ are given in Fig. 5. The intrusion towards the interior of the source water, leaving the incline is clearly visible. The cyclonically progressing deep boundary current is seen by the isolines of the tangential velocity $\langle u_{\hat{\phi}} \rangle_\phi$. Note that the distance of the centre of the current is located at a horizontal distance of about $l_{\text{deep}} = 70$ cm from the intrusion point, which is much larger than $l_{\text{iner}} = 91$ cm (where we used Eq. (11) and $b_{\text{in}} = 5 \cdot 10^{-2}\text{m s}^{-2}$, see Fig. 5) and the deep current be explained by an inertial overshoot. It is also interesting to note that the deep boundary current of exp42 is not squeezed to the boundary, there are no strong velocity gradients or boundary layers associated to it. This indicates that the boundary current is not subject to strong frictional processes a friction time can be estimated as $t_{\text{deep}} = l_{\text{deep}}^2/\nu \approx 5 \cdot 10^5$ s, much longer than the duration of the experiment. The interfacial friction is however strong enough to sustain an interfacial Ekman layer responsible for the intrusion. This is clearly visible in Fig. 5 where the bottom Ekman layer leaves the boundary and proceeds in the interior as an interfacial Ekman layer. The velocities in the interfacial Ekman layer are almost an order of magnitude smaller than in the bottom Ekman layer and its strength decreases as it penetrates to the interior. At the top of the intruding current there is another Ekman layer in which the transport is directed towards the boundary. The averaged radial velocities $\langle u_r \rangle_\phi$ are small, typically two orders of magnitude smaller than the averaged tangential velocities $\langle u_{\hat{\phi}} \rangle_\phi$. The persistence of the interfacial Ekman layer does not contradict the findings of [29], where it was shown that Ekman layers disappear when the system is freely evolving, that is far from a boundary. For the highest rotation case $l_{\text{iner}} = 1.4$ cm and the deep boundary current is

squeezed against the boundary and the Ekman layer does not separate from the boundary (see Fig. 6).

We observe that the square of the intruding distance along the interface is proportional to time, $x^2 \propto t$, as demonstrated in Figs. 7 and 8, where a clear scaling is observed for at least one decade, for all experiments with rotation. In both figures the time is counted from the arrival of the corresponding s-value at the point from which the current intrudes. The scaling is illustrated in Fig. 7 for exp02 using different values of σ_S. In Fig. 8 results from experiments for one value of σ_S for each experiment performed is presented. The non-rotating case exp22 also shows the scaling behaviour. Due to the oblique injection at 45^o the fluid is rotating and the dynamics has an effective Coriolis frequency, which is however low and varies in space and time. For the faster rotating cases (exp12 and exp32) the scaling is no-longer observed for approximately $t > 1000$ s as the gravity current changes from Ekman layer dynamics to cascading. More precisely the intruding current proceeds faster than $x \sim \sqrt{t}$ resembling a linear growth $x \sim t$ for exp032 from t =1000 to 2000 s (see Fig. 8).

In section 3 we showed, that not only the increase of the intrusion scales with time, but also the rate of increase (the offset of the graphs corresponding to different experiments in Fig.8) has a dimensional scaling of $\gamma \sim f^{-1}$. This scaling is observed between the two lower rotation cases, but breaks down when considering the faster rotating cases. This is no surprise as we have seen that the downslope regime changes qualitatively with the rotation rate for the higher rotation cases, going from Ekman dynamics to cascading. Scaling behaviours can only be expected when the same dynamic regime prevails.

6.3. Recirculation

The dynamics extending from above the gravity current to the surface is not subject to frictional processes and turbulent fluxes are negligible, when the gravity current circulation is sub-critical. Furthermore, the abundant internal waves have only a weak direct influence on the recirculation. A maximal Rossby number of the recirculation can be calculated by calculating $\epsilon = \max(2\langle u_{\hat{\phi}} \rangle_\phi / (fr))$

for $r \geq 6$m. In all experiments with rotation and for the duration of the experiments investigated we have $\epsilon < 0.2$, well within the regime of quasi-geostrophy.

This is demonstrated by Fig. 9, which shows that the conservation of potential vorticity using averaged variables only, allows to explain the recirculation. The figure gives the approximated potential vorticity balance of Eq. (15), neglecting the horizontal advection of potential vorticity (last term in the equation). More precisely, the layer between a depth of -0.15 m and -0.01 m is considered. In this figure the l.h.s of Eq. (15) and the spatial averaged r.h.s superpose within statistical error for exp02 at $t = 1500$ s and 3000 s, for $0 \leq r \leq 5.5$ m. This shows that this part is well described by the conservation of potential vorticity and that fluctuations and turbulent fluxes can be neglected. The noisiness of the black line is due to the sensitivity of the vertical velocity to gravity waves, which leave their signature even in the averages $\langle w(-h_0)\rangle_\phi$. For higher values of $r > 5.2$ m the approximation fails due to the strong eddy-activity and the associated turbulent fluxes. Furthermore, in the vicinity of the source points strong downward velocities occur and the concept of shallow-water potential-vorticity is no-longer applicable. Comparing both panels in Fig. 9 shows that the magnitude of the tangential velocity increases with time as predicted for a continuous forcing by the vertical velocity. The recirculation does not attain a stationary state. When the (negative) tangential velocity becomes smaller than the negative of the geostrophic velocity just above the Ekman layer, as seen at $t = 3000$ and $r = 5.$ m in exp32 (green line in left lower panel of Fig. 4), the transport in the Ekman layer is directed upslope (see discussion in the previous subsection).

The approximation for the potential vorticity conservation is observed for the lower rotation rates for the times of the integration, but breaks down when the rotation rate is increased or at later integration times due to the intermittent cascading dynamics influencing the recirculation.

6.4. Interaction of gravity current, intrusion and recirculation

The gravity current dynamics decides on the downward volume and buoyancy transport. The amount of volume and buoyancy that arrives at the intrusion point governs the dynamics of the deep boundary current. Both, the gravity current and the intruding dynamics lead to a compression of the super-posing water-column, the water above reciculates outward and turns anti-cyclonically at an increasing rate. During this process the thermal wind balance prevails. When the tangential velocity above the gravity current exceeds the geostrophic velocity, the geostrophic pressure gradient pushes the water upslope in the Ekman layer. This can be seen in lower right panel of Fig. 4, where at $r = 5$ m the Ekman transport is clearly inverted, upslope. The downward buoyancy transport passes from a laminar Ekman dynamics to cascading down the incline above the Ekman layer.

7. Discussions

We have performed a series of numerical experiments on a configuration of buoyancy driven flows, varying the densification rate and the rotating rate. The circular symmetry and the high number of sources allow for averaging along the angle ϕ and mathematically separating the dynamics in a circulation and fluctuations, where both are evolving in time. The purpose of the experiment is to not only describe the different processes involved (gravity current, intrusion and recirculation) but also their interaction.

We found a qualitative change in the gravity current going from the Ekman dynamics, when the buoyancy production rate is lower than the maximal buoyancy Ekman transport, to the cascade dynamics when it is higher. This prevents a clear scaling of the observed quantities with the rotation rate and the buoyancy production rate.

When the gravity current water reaches the interface it intrudes along the interface between a denser and a lighter water mass. The intrusion can be explained by an inertial overshoot and leads to a deep boundary current that is

well separated from the incline in the lower rotation case, while it stays attached to the boundary in the fast rotating cases. In the former case, the dynamics of the deep boundary current is not subject to strong boundary friction. Over at least one decade in time, the intrusion of the gravity current water proceeds at a rate that is proportional to $\sqrt{t}$, for the rotating cases. In the faster rotating cases the scaling behaviour disappears when the cascading reaches the interface and the propagation increases, resembling a linear scaling for the fastest rotation. This can probably be explained by the appearance of coherent dipole structures that resemble hetons ([30]), transporting buoyancy anomalies in a ballistic way away from the incline. Research with simulations dedicated to this subject will be performed in the near future. The intrusion of source water does not proceed at a constant velocity and can be called non-intruding.

When the buoyancy transport is performed by the Ekman transport, the recirculation leads to a continuous increase of the anti-cyclonic tangential velocity in the upper layer, which results in a blockage of the buoyancy transport in the Ekman layer below and the gravity current dynamics passes to a cascade dynamics. In our configuration with a continuous densification, the dynamics will at one point become a cascade dynamics and turbulent due to the retroaction of the recirculation dynamics on the gravity current. A counter current at the surface at the downslope side of the gravity current can lead to an upslope Ekman transport and the gravity current cascades down the incline in a thickened bottom boundary layer. The dynamics in the experiment is rich due to the interaction of the different phases.

It is important to note that in the case without rotation the oblique acceleration at the source points leads to a cyclonic circulation in most of the domain and the circulation has an effective f, which is however small, strongly varying in space and time. The circulation is qualitatively different as rotation does not constraint the thickness of the downslope gravity current and it descends as a non-rotating gravity current. The intruding current is not confined to the slope and the recirculation of the water above is not influenced by rotation.

8. Conclusions

The dynamics in the present experiment evolves on a large range of scales, from basin-scale circulation, to the synoptic eddies, the sub-mesoscale processes that approach a 3D turbulent behaviour, mixing, diffusion and down to the Ekman dynamics due to viscous friction at the smallest scales. The dynamics also shows an abundance of internal waves, which are not discussed here.

For the experiments evolving in a rotating frame, we showed that the basin wide circulation is always close to geostrophic away from the boundaries, but this does not mean that the evolution is quasi-geostrophic. Quasi-geostrophy relies on the conservation of potential vorticity. It is the dynamics that is observed when the geostrophy is perturbed by non-linearity, a spatially varying Coriolis parameter, small variations of topography and variations in the vertical stratification (see [31]). These perturbations act from the basin scale to the synoptic scale. In the here presented circulation, however, the evolution of the geostrophic equilibrium is determined by sub-mesoscale, 3D-turbulent and diffusive processes. When these diabatic processes perturb the geostrophic equilibrium, potential vorticity is not conserved and the dynamics is not quasi-geostrophic. It is a circulation which we here call sub-quasi-geostrophic. We refer the reader to [32] for a rigorous discussion of the effect of diabatic processes on the potential vorticity. More precisely, it is important to note that the circulation of the tangential velocity and the radial density gradient observe the thermal-wind relation, away from the boundaries, while the dynamics in the radial dynamics is governed by 3D-turbulence and friction. It is the radial dynamics which is neither geostrophic nor quasi-geostrophic that determines the temporal evolution of the circulation. The experiment allows the separation in tangential and radial part and the averaging along a homogeneous direction, ϕ. This permits to evaluate the effect of sub-quasi-geostrophic processes on the geostrophic circulation.

Acknowledgements We are grateful to Francis Auclair, Lucie Bordois and Franck Dumas for discussion. The work was funded by Shom, contract

N 20CP03.

References

[1] J. E. Simpson, Gravity currents in the laboratory, atmosphere, and ocean, Annual Review of Fluid Mechanics 14 (1982) 213–234.

[2] R. Griffiths, Gravity currents in rotating systems, Annual Review of Fluid Mechanics 18 (1986) 59–89.

[3] A. Wåhlin, G. Walin, Downward migration of dense bottom currents, Environmental Fluid Mechanics 1 (2001) 257–279.

[4] J. J. Monaghan, Gravity current interaction with interfaces, Annu. Rev. Fluid Mech. 39 (2007) 245–261.

[5] P. G. Baines, Mixing in downslope flows in the ocean-plumes versus gravity currents, Atmosphere-ocean 46 (2008) 405–419.

[6] A. Wirth, On the basic structure of oceanic gravity currents, Ocean dynamics 59 (2009) 551–563.

[7] M. O. Baringer, J. F. Price, A review of the physical oceanography of the mediterranean outflow, Marine Geology 155 (1999) 63–82.

[8] W. E. Johns, S. S. Sofianos, Atmospherically forced exchange through the bab el mandeb strait, Journal of physical oceanography 42 (2012) 1143–1157.

[9] S. Pous, X. Carton, P. Lazure, Hydrology and circulation in the strait of hormuz and the gulf of oman—results from the gogp99 experiment: 2. gulf of oman, Journal of Geophysical Research: Oceans 109 (2004).

[10] L. Umlauf, L. Arneborg, H. Burchard, V. Fiekas, H. Lass, V. Mohrholz, H. Prandke, Transverse structure of turbulence in a rotating gravity current, Geophysical Research Letters 34 (2007).

[11] R. H. Käse, J. B. Girton, T. B. Sanford, Structure and variability of the denmark strait overflow: Model and observations, Journal of Geophysical Research: Oceans 108 (2003).

[12] I. Fer, G. Voet, K. S. Seim, B. Rudels, K. Latarius, Intense mixing of the faroe bank channel overflow, Geophysical Research Letters 37 (2010).

[13] M. Flexas, X. D. De Madron, M. Garcia, M. Canals, P. Arnau, Flow variability in the gulf of lions during the mater hff experiment (march–may 1997), Journal of Marine Systems 33 (2002) 197–214.

[14] G. Shapiro, A. Zatsepin, Gravity current down a steeply inclined slope in a rotating fluid, in: Annales Geophysicae, volume 15, Copernicus GmbH, pp. 366–374.

[15] C. Cenedese, J. A. Whitehead, T. Ascarelli, M. Ohiwa, A dense current flowing down a sloping bottom in a rotating fluid, Journal of Physical Oceanography 34 (2004) 188–203.

[16] S. Davarpanah Jazi, M. G. Wells, J. Peakall, R. M. Dorrell, R. E. Thomas, G. M. Keevil, S. E. Darby, J. Sommeria, S. Viboud, T. Valran, Influence of coriolis force upon bottom boundary layers in a large-scale gravity current experiment: Implications for evolution of sinuous deep-water channel systems, Journal of Geophysical Research: Oceans 125 (2020) e2019JC015284.

[17] A. Rubino, M. Gačić, M. Bensi, V. Kovačević, V. Malačič, M. Menna, M. E. Negretti, J. Sommeria, D. Zanchettin, R. V. Barreto, et al., Experimental evidence of long-term oceanic circulation reversals without wind influence in the north ionian sea, Scientific reports 10 (2020) 1–9.

[18] Y. S. Chang, T. M. Özgökmen, H. Peters, X. Xu, Numerical simulation of the red sea outflow using hycom and comparison with redsox observations, Journal of physical oceanography 38 (2008) 337–358.

[19] S. Legg, B. Briegleb, Y. Chang, E. P. Chassignet, G. Danabasoglu, T. Ezer, A. L. Gordon, S. Griffies, R. Hallberg, L. Jackson, et al., Improving oceanic

overflow representation in climate models: the gravity current entrainment climate process team, Bulletin of the American Meteorological Society 90 (2009) 657–670.

[20] N. Laanaia, A. Wirth, J.-M. Molines, B. Barnier, J. Verron, On the numerical resolution of the bottom layer in simulations of oceanic gravity currents, Ocean Science 6 (2010) 563–572.

[21] E. Yankovsky, S. Legg, Symmetric and baroclinic instability in dense shelf overflows, Journal of Physical Oceanography 49 (2019) 39–61.

[22] M.-E. Negretti, , F. Tucciarone, A. Wirth, Intruding gravity currents on the coriolis plateform, draft (2021).

[23] J. M. Huthnance, Accelerating dense-water flow down a slope, Journal of physical oceanography 39 (2009) 1495–1511.

[24] M. V. Luneva, V. V. Ivanov, F. Tuzov, Y. Aksenov, J. D. Harle, S. Kelly, J. T. Holt, Hotspots of dense water cascading in the arctic ocean: Implications for the pacific water pathways, Journal of Geophysical Research: Oceans 125 (2020) e2020JC016044.

[25] A. Rubino, D. Romanenkov, D. Zanchettin, V. Cardin, D. Hainbucher, M. Bensi, A. Boldrin, L. Langone, S. Miserocchi, M. Turchetto, On the descent of dense water on a complex canyon system in the southern adriatic basin, Continental Shelf Research 44 (2012) 20–29.

[26] A. Dai, C.-S. Wu, High-resolution simulations of cylindrical gravity currents in a rotating system, Journal of Fluid Mechanics 806 (2016) 71–101.

[27] A. Dai, C.-S. Wu, High-resolution simulations of unstable cylindrical gravity currents undergoing wandering and splitting motions in a rotating system, Physics of Fluids 30 (2018) 026601.

[28] A. F. Shchepetkin, J. C. McWilliams, Computational kernel algorithms for fine-scale, multiprocess, longtime oceanic simulations, in: Handbook of Numerical Analysis, volume 14, Elsevier, 2009, pp. 121–183.

[29] A. Wirth, On the vanishing of the interfacial ekman layer, Journal of physical oceanography 41 (2011) 1035–1040.

[30] N. Hogg, H. M. Stommel, The heton, an elementary interaction between discrete baroclinic geostrophic vortices, and its implications concerning eddy heat-flow, Proceedings of the Royal Society of London. A. Mathematical and Physical Sciences 397 (1985) 1–20.

[31] G. K. Vallis, Atmospheric and oceanic fluid dynamics, Cambridge University Press, 2017.

[32] Y. Morel, J. Gula, A. Ponte, Potential vorticity diagnostics based on balances between volume integral and boundary conditions, Ocean Modelling 138 (2019) 23–35.

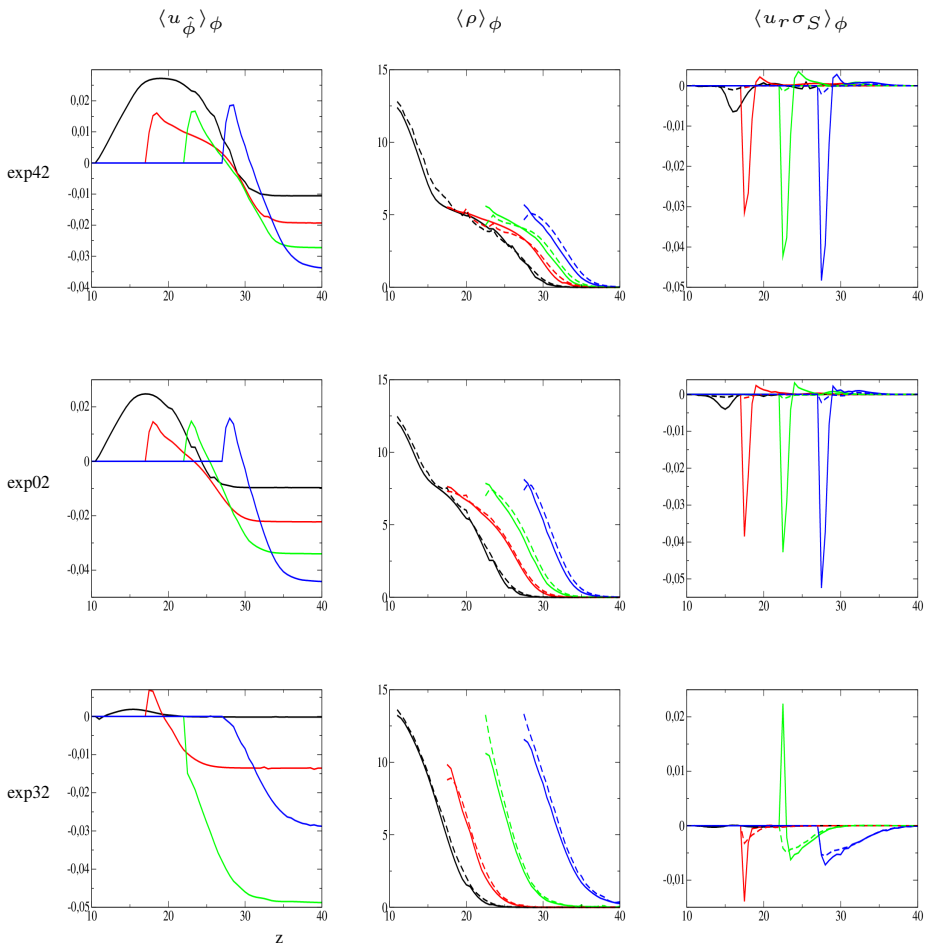

Figure 4: Upper figs. are for exp42 and $\tilde{t} = 12.5$ days, middle figs. are for exp02 and $\tilde{t} = 25$ days, lower figs. are for exp32 and $\tilde{t} = 100$ days (days measured in rotation periods, dimensional time is $t = 3000$ s for all experiments) Data plotted as a function of the vertical coordinate between z=0.1 and 0.4 m, at r=3.82 m (black lines), r=4.48 m (red lines), r=5.0 m (green lines)and r=5.53 m (blue lines). Left: $\langle u_{\hat{\phi}} \rangle_\phi$. Middle: $\langle \rho \rangle_\phi$, dashed lines show the density calculated using the tangential velocity $\langle u_{\hat{\phi}} \rangle_\phi$ and the thermal wind relation (eq. 3). The good correspondence shows the geostrophy is observed. Right: total ($\langle u_r \sigma_S \rangle_\phi$, full lines) and fluctuating ($\langle u_r s \rangle_\phi - \langle u_r \rangle_\phi \langle \sigma_S \rangle_\phi$, dashed lines) radial salinity-transport averaged along the angle ϕ.

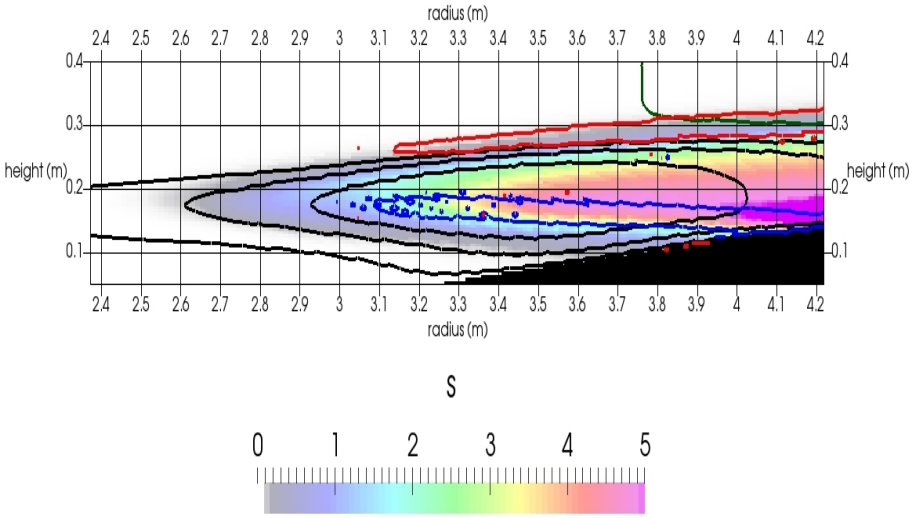

Figure 5: Exp42: the colour code shows the density anomaly of the source water $\langle s \rangle_\phi$. Dense water of layer 2 is not shown. Black lines are isolines of $\langle u_{\hat{\phi}} \rangle_\phi$ for 0.01, 0.02 and 0.03 m s^{-1} and green for -0.01 m s^{-1}. Isolines of $\langle u_r \rangle_\phi$ are blue for -3. 10^{-4}m s^{-1} and red for 3. 10^{-4} m s^{-1} show the Ekman layers.

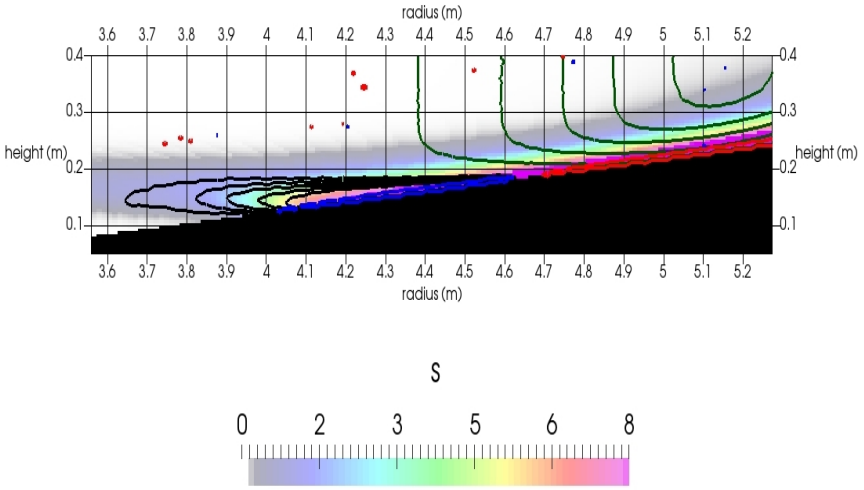

Figure 6: Density anomaly of the source water $\langle s \rangle_\phi$ for exp32. Dense water of layer 2 is not shown. Isolines of $\langle u_{\hat{\phi}} \rangle_\phi$ are black for 0.001, 0.002 and 0.003 m s^{-1} and green for -0.01, -0.02 and -0.03 m s^{-1}. Isolines of $\langle u_r \rangle_\phi$ are blue for -3. 10^{-4}m s^{-1} and red for 3. 10^{-4} m s^{-1} show the Ekman layers.

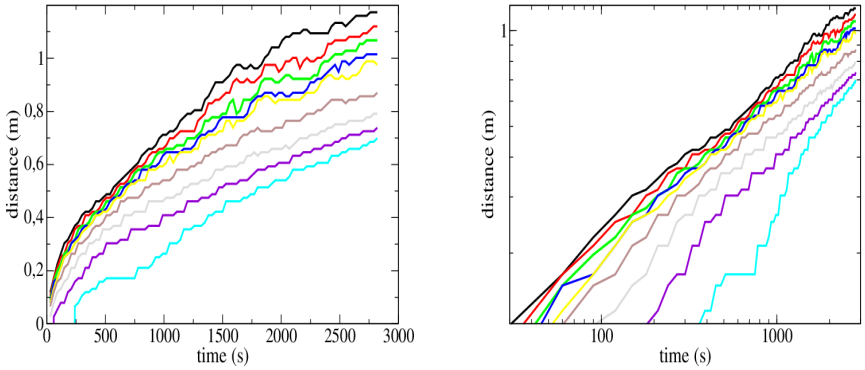

Figure 7: Progression of the density front in exp02, for different values of $\sigma_S = 0.1$ (black), 0.2 (red), 0.3 (green), 0.5 (blue), 1.0 (yellow) and 2.0 (brown). The horizontal axis measures time from the arrival of the gravity current and the vertical axis is the horizontal distance from the incline from the point where the vein of the gravity current penetrates to the interior. Right figure is in log-log. Note that all curves in the log-log plot have a slope close to 1/2, the diagonal in the figure.

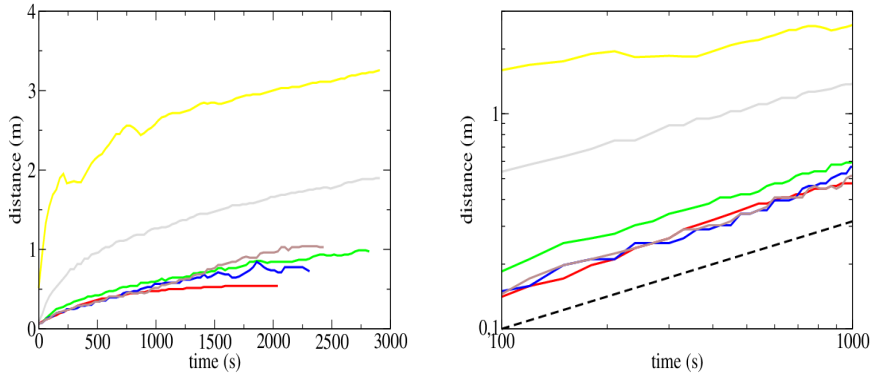

Figure 8: Progression of the density front (for salinity $\sigma_S = 0.005$ for exp00 and $\sigma_S = 0.5$ for other experiments) and different experiments: exp00 (red), exp002 (green), exp012 (blue), exp022 (yellow) , exp032 (brown) and exp042 (grey). Dashed black line gives scaling of 1/2.

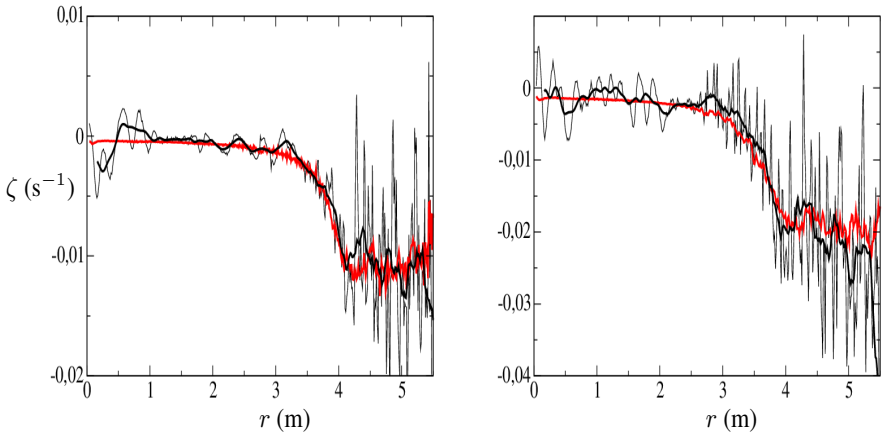

Figure 9: Potential vorticity analysis in exp02. The curves are the l.h.s (tick red) and r.h.s (thin black) of Eq. (15) integrated from t=240 s to 1500 s (left) and 3000 s (right) (i.e. $\zeta(t = 3000\text{ s}, r) - \zeta(t = 240\text{ s}, r)$ for l.h.s. in s^{-1}) as a function of the radius. The thick black line is a 20 point average of the thin black line.